Regular Article - Living Systems

Measuring the average cell size and width of its distribution in cellular tissues using Fourier transform

Tess Homan[1], Sylvain Monnier[1], Cécile Jebane[1], Alice Nicolas[2,a], and Hélène Delanoë-Ayari[1,b]

[1] Univ Lyon, Univ Claude Bernard Lyon 1, CNRS, Institut Lumière Matière, 69622, Villeurbanne, France
[2] Univ. Grenoble Alpes, CNRS, CEA/LETI-Minatec, Grenoble INP, LTM, 38054 Grenoble, France

Abstract We present an in-depth investigation of a fully automated Fourier-based analysis to determine the cell size and the width of its distribution in 3D biological tissues. The results are thoroughly tested using generated images, and we offer valuable criteria for image acquisition settings to optimize accuracy. We demonstrate that the most important parameter is the number of cells in the field of view, and we show that accurate measurements can already be made on volume only containing $3 \times 3 \times 3$ cells. The resolution in z is also not so important, and a reduced number of in-depth images, of order of one per cell, already provides a measure of the mean cell size with less than 5% error. The technique thus appears to be a very promising tool for very fast live local volume cell measurement in 3D tissues in vivo while strongly limiting photobleaching and phototoxicity issues.

1 Introduction

Cellular volume is a key parameter in various fundamental biological processes such as cell growth, division or fate [1,2]. It is tightly regulated during cell cycle [1], depends on the chemical and physical properties of the cell's microenvironment [2,3] and can be regulated by cellular tension [4]. Different techniques have been developed to measure the volume of isolated cells such as 3D cell reconstruction [2], fluorescence exclusion measurements [5] and commercial coulter counter [6]. However, so far the regulation of cellular volume within 2D/3D tissues remains unknown, which is a brake for our understanding of tissue homeostasis. This is mainly due to technical limitations associated with the measurement of cellular volume inside a tissue and its follow-up in time. Indeed, obtaining cellular volume requires a precise segmentation of the cell boundaries in 3D. Consequently, it is most often necessary to acquire a 3D stack of a sample in which the membrane [7] or intercellular space [8] is fluorescent. However, at high resolution, the amount of images which can be acquired to create a 3D stack is experimentally limited. Specifically, it is either limited by the acquisition speed of the entire stack (up to several minutes) which is on the same timescale as cell movements inside tissue or by the amount of light cells can experience without photobleaching and/or being damaged. Therefore, developing a new tool which would require the minimum z slices

acquisition is of real importance for time follow-up of in vivo tissues.

Based on previous work [9], we propose here a 3D Fourier transform analysis tool for live measurement of cell volume within 3D tissues. Fourier analysis describes an image as a superposition of sinusoidal functions (repetitive patterns with a set frequency) [10]. Cohesive tissues have the feature of being a tight assembly of similar units, cells, and the resulting Fourier analysis consequently displays one dominant frequency corresponding to the average cell size. Here, we tested the accuracy of the Fourier analysis by using *in silico* simulated data of 3D tissues. This allowed us to independently vary all important parameters, such as the number of cells in field of view, cell size homogeneity and acquisition resolution. Based on this analysis, we propose protocols to help define image acquisition parameters. We further validated our Fourier analysis method on live cell aggregates images, which represent good in vitro tumor models [11].

2 Materials and methods

2.1 Cellular aggregates preparation

We use HT29 cells for these experiments. Cells are culture in DMEM (GIBCO, 61958-026) supplemented with 10% FBS (Pan Biotech, P308500) and 1% penicillin–streptavidin (GIBCO, 15140-122). They are maintained at 37°C with 5% CO_2 and passaged twice a week. Aggregates are formed using Ultra Low Adhesion 96

---

[a] e-mail: alice.nicolas@cea.fr
[b] e-mail: helene.ayari@univ-lyon1.fr (corresponding author)

Well Plates (Greiner Bio-One, 650970). After passaging, cells are counted and diluted to a concentration of 10,000 cells/mL. From this stock solution, a desired number of cells are subsequently seeded into a well (for example 300 cells/mL) and left to grow into aggregates for a minimum of 48 h.

2.2 Two-photon imaging of cellular aggregates and application of osmotic shocks

Aggregates were imaged either in simple wells with #1 coverslip at the bottom or in $40\,\mu$m-high microfluidic channel. Entrapment in the microfluidic channel prevented aggregates from moving around and simplified media changes. One hour after the injection of the aggregates in the well or in the microfluidic chamber, the extracellular space was stained with FITC-Dextran diluted at 2 mg/mL, thus staining the interstitial fluid within the aggregate. All experiments were conducted at 37^oC in CO_2-independent cell culture medium (GIBCO, 18045-088). Imaging was performed using a two-photon setup on a Nikon microscope equipped with a 780-nm laser. Osmotic shocks were applied by adding 6 kDa Dextran at a concentration of 100 g/L (for details see [12]).

2.3 Artificial cell images generation

Synthetic 3D images of size $L \times L \times L$ pixels mimicking real tissues were generated. Random points (representing the centers of the cells) are added automatically one after the other in a 3D matrix. For each new point, a radius is randomly taken from a normal distribution centered on r_0 with a width σ. A new point, i, is only added in the lattice if the sphere centered on i with radius $r(i)$ fits in with all other spheres. If not, a new random point is chosen. When the number of spheres increases, the probability that the new sphere fits in the free space decreases. We thus used as a cutoff a maximum number of attempts to add a cell. Note that as the space has a very low probability of being fully filled with compact spheres, the obtained lattice is not regular even when σ is set to 0. The width of the size distribution was adjusted in two ways, either by changing σ or by changing the number of possible attempts for filling the lattice. As r_0 defines the typical number of pixels per cell, changing this value enabled to simulate different magnifications used when acquiring real data with different objectives at different resolutions. The total number of cells that are visible in the image were set by changing L, which corresponds to changing the field of view in data acquisition. To avoid edge effects, the actual space in which the centers were distributed runs from $-2r_{\max}$ to $L+2r_{\max}$ in x, y, and z-direction. The images were then cut out from the center to create an $L \times L \times L$ 3D stack.

Cell boundaries were then generated. More precisely, a 3D Voronoi tessellation was performed, using cell centers as seeds. As experimentally the cells edges or faces are larger than 1 pixel (Fig. 1a), the gray values of the pixels in every Voronoi cell were scaled with the relative distance to the seed. This allowed obtaining a 3D image much closer to real data (Fig. 1b). Amira software was used to segment and visualize the simulated data (Fig. 1c).

2.4 Fourier transform analysis

Fourier transformation was used to analyze the intensity of the 3D images. The Fourier transform of the intensity is expected to resemble the diffracted intensity in an isotropic medium scattered by elastic processes. Before applying Fourier transform, the images were decomposed in periodic (p) and smooth components (s). The Fourier transform was applied on p only to avoid edge effects artifacts [13]. The discrete Fourier transform (DFT) was computed using a fast Fourier transform (FFT) algorithm [14] with convention:

$$\tilde{I}(\mathbf{k}) = \sum_{l,m,n=0}^{L-1} I(\mathbf{x}) \exp(-2i\pi \mathbf{k} \cdot \mathbf{x}) \qquad (1)$$

with I the intensity, $\mathbf{x}$ the discrete position indexed by (l, n, m) and $\mathbf{k} = 1/L * (s, t, u)$ the discrete wave vector (L being dimensionless).

Consistent with elastic diffusion processes of slightly ordered isotropic materials, a bright shell around an even brighter center pixel was obtained (Fig. 1d). We expect that the radius of the shell, k_D, can be used to obtain an estimation of the averaged cell diameter. To properly determine k_D, we took advantage of the spherical symmetry of the FFT. $\tilde{I}$ was interpolated in spherical coordinates (k, θ, ϕ). The normalized power spectral density of the cell aggregate is calculated:

$$e_n(k) = \frac{k^2 \int |\tilde{I}(\mathbf{k})|^2 \sin \theta \, d\theta \, d\phi}{\int |\tilde{I}(\mathbf{k})|^2 d\mathbf{k}} \qquad (2)$$

Different from conventions used in the analysis of elastic diffusion of light, Eq. (2) is normalized by the total power spectral density and not by the spectral volume. $e_n(k)$ then shows well-emerged peaks that we considered to determine the average cell size in the tissue (Fig. 1f).

2.5 Local Fourier transform measurements

We performed local cell measurements on spheroid compressed in between two plates (cylindrical geometry Fig. 9a). First, we determined the radius and center of the base of the cylinder using a global thresholding of the aggregate and fitting the contour of this binary image with a circle. Next, we divide our image in subimages centered on a polar grid (r, θ), and we run the Fourier analysis on each of this subimage and then average over θ, to get the cell size as a function of the radial distance to the aggregate center.

All the codes necessary for running this global or local analysis are freely available on github.
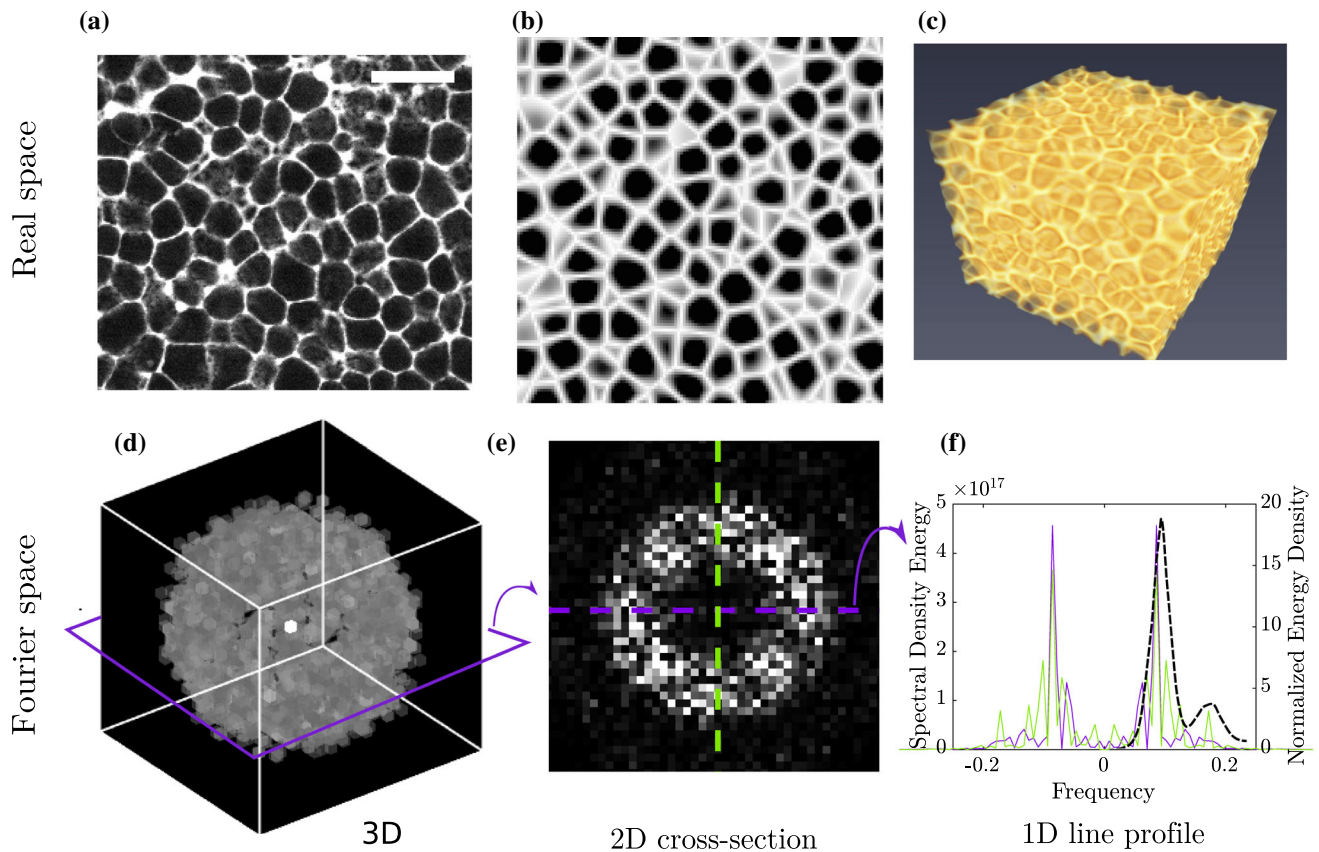
Fig. 1 **a** Typical z-slice of an HT29 aggregate using two-photon acquisition. Bar: 30 µm. **b** Z-slice (128 × 128 pixels) of a simulated 3D aggregate generated using the Voronoi method. The cells have an average radius of 11 pixels. Note that faces parallel to the z-slice can result in large white areas. **c** 3D rendering of the entire simulated 3D stack from **b** where $dz = 1$ pixel, i.e., the same resolution as in x, y. **d** Fourier transform of **c**. A bright center pixel and a light spherical shell are visible. **e** 2D cross section of **d**. The magnitude of the central peak is set to zero for rendering purposes. **f** Spectral density energy along the purple and green dashed line displayed in **e**. The black dashed line is the normalized power spectral density $e_n(k)$ as defined in Eq. (2). The position of the main black peak provides an accurate measurement of the mean cell size

2.6 Calculation of cell form and structure factors

The scattering pattern should be linked to a cell form factor that informs on the mean symmetry properties of the cells and a structure factor that informs on the cellular arrangement. We calculated both factors independently on simulated images. Cells that were entire in the image volume (not cut by the borders) were considered. The centroid of the cells (which could differ from the points used to generate the Voronoi tessellation) was extracted, and masks were generated to display each cell individually. The power spectral density was calculated for each single cell as in Eq. (2). The cell-averaged power spectral density of the single cells was then obtained:

$$e_{n,cell}(k) = N_{cell} \frac{< k^2 \int_{cell_i} |\tilde{I}(\mathbf{k})|^2 \sin\theta \, \mathrm{d}\theta \, \mathrm{d}\phi >_{cells}}{\int |\tilde{I}(\mathbf{k})|^2 \mathrm{d}\mathbf{k}}$$

(3)

with N_{cell} the number of entire cells in the image.

3 Results on simulated 3D aggregates

Using simulations on 3D aggregates, we will now show that our Fourier analysis technique is a good tool for measuring accurately the width and the average of the cell size distribution. We will show how the Fourier peak is arising from the combination of the form factor of individual cells inside the aggregate and from the structure factor (linked to their spatial organization in 3D). We will finally test the robustness of our analysis as a function of the acquisition parameters usually used in real data imaging.

3.1 Cell sizes

Figure 1d–e shows an isotropic diffusion pattern, suggesting that the cells are only weakly ordered in the aggregate. The radius of the shell should then provide the mean distance in between cells. Hence, we will show that this length corresponds to the diameter of individual cells in 3D compact aggregates as we address here.
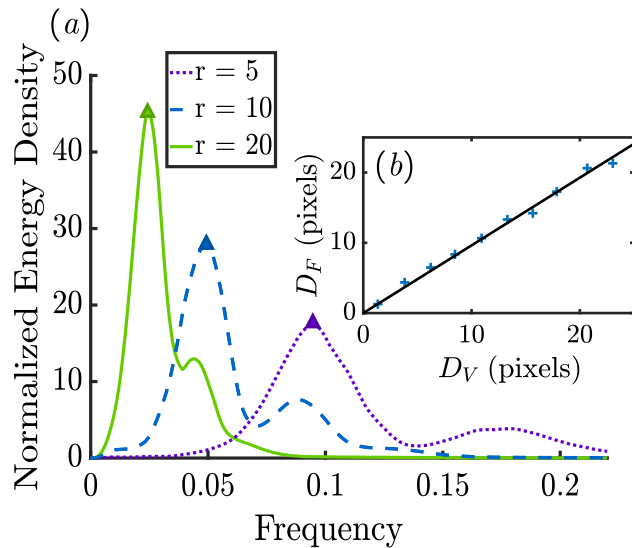
Fig. 2 The Fourier analysis accurately predicts the size of cells from simulated data. **a** Curves resulting from the Fourier analysis for three different values of r_0, $\sigma = 0$, $L = 128$. Position of the peaks corresponds to the frequency or wavelength of the artificial tissue. **b** Plot of D_F as a function of the original D_V, with an affine fit with a slope of 0.96 ($r^2 = 0.992$)

As the relationship between cell distance (D_F) and the position of the frequency peak ($k_{\max}$) is very sensitive to the accuracy of the model used to describe the cell aggregate [15], we first defined $D_F = \gamma/k_{\max}$ with γ a factor of proportionality. We compared the value of cell size computed with the peak of the normalized Fourier energy density to the known average size of cells from simulated data. However, even though for the original data the exact locations of all cell walls are known, it is still not trivial to define an average cell size. From the Voronoi tessellation, we easily retrieved the volume of each cell (completely enclosed in the image), whose averaged value is denoted V. Thus, the average diameter was obtained from dimensional analysis: $D_V = \lambda V^{1/3}$, the proportionality factor λ depending on the precise mean morphology of the cells. Changing the cell shape from spherical to cubical would alter the calculation of the diameter by 30%. Besides, since the cell contour is always included when computing the cellular volume, we will more precisely use $D_V = \lambda V^{1/3} - 1$ (pixels) so that the contour is not counted twice in the distance between two cells.

Several values of r_0, the mean radius of the Voronoi cells, were tested (Fig. 2). The Fourier peak was both wider and lower with increasing cell size because of finite size effects in the Fourier transformation. Figure 2b shows that the measure from the Fourier analysis correlates very well with the direct measure from the Voronoi cells when choosing $\gamma = 1$ and $\lambda = 1$ (slope 0.96, coefficient of determination 0.992).

3.2 Relation between the energy spectral density, the structure factor and the cell form factor

The form and structure factors are generally deduced from diffusion patterns and help characterize the organization of matter. Here, we tested if we could deduce values for these two factors from the spectral energy densities introduced in Eqs. (2) and (3). The power spectral density can be calculated analytically for a 3D aggregate constituted of N_{cells} within the approximation of isotropic material. We denote $f_j(\mathbf{r})$ the fluorescence intensity due to cell j. Within the approximation that all cells have the same intensity profile $f(\mathbf{r})$, the total intensity is:

$$I(\mathbf{r}) = \sum_{j=1}^{N_{cell}} f(\mathbf{r} - \mathbf{r_j}) \tag{4}$$

with $\mathbf{r_j}$ the center of cell j. The square norm of the Fourier transform coefficients of $I(\mathbf{r})$, $\tilde{I}(\mathbf{k})$ then writes:

$$|\tilde{I}(\mathbf{k})|^2 = N_{cell} * |\tilde{f}(\mathbf{k})|^2 S(\mathbf{k}) \tag{5}$$

with $S(\mathbf{k}) = \frac{1}{N_{cell}} \sum_{j=1}^{N_{cell}} e^{-2\pi i \mathbf{k}.(\mathbf{r}_j - \mathbf{r}_k)}$ and $|\tilde{f}(\mathbf{k})|$, respectively, the structure and form factor of the cell. Averaging over all angles, and if $S(\mathbf{k})$ and $|\tilde{f}(\mathbf{k})|$ are uncorrelated, the power spectral density reads as:

$$e_n = e_{n,cell}(k) \cdot S(k) \tag{6}$$

with

$$e_{n,cell} = \frac{4\pi N_{cell} k^2 |\tilde{f}(k)|^2}{\int |\tilde{I}(\mathbf{k})| \mathrm{d}\mathbf{k}} \tag{7}$$

being the averaged power density of all individual cells renormalized by the total spectral density of the image and $S(k) = \int S(\mathbf{k}) \sin\theta \, d\theta \, d\phi$ the integrated structure factor on a shell of radius k. Figure 3b shows the integrated structure factor calculated for the cells in the simulated data. The latter shares similarities with the structure factor of a hard sphere fluid [16], but still appears more complex. This suggests that the interaction potential between the cells requires refinement compared to volume exclusion. Unfortunately, both the cell form (Fig. 3c) and structure factors (Fig. 3b) cannot be obtained analytically as it could have been the case for simpler geometries and known interactions (see [17] for a review of well-known cases where models do exist).

The power spectral density was fitted using Eq. (6). This could only be done by introducing two constants, α and β, that evidenced an affine relationship between e_n and $e_{n,cell}$:

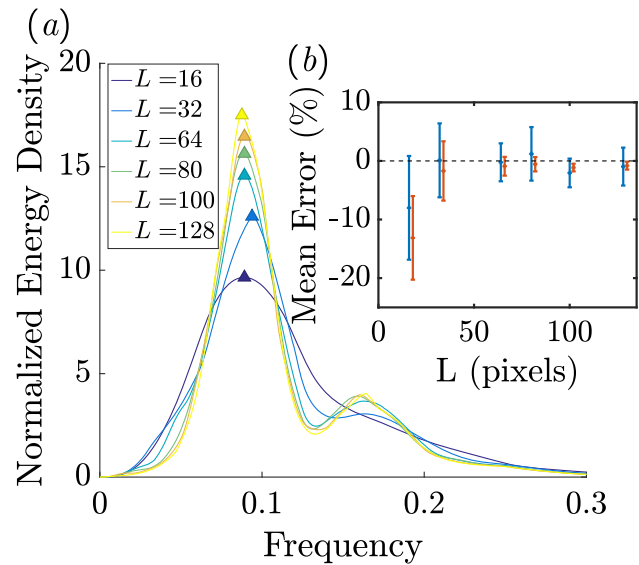$$e_n(k) = \alpha e_{n,cell}(k) \cdot S(k) + \beta \tag{8}$$
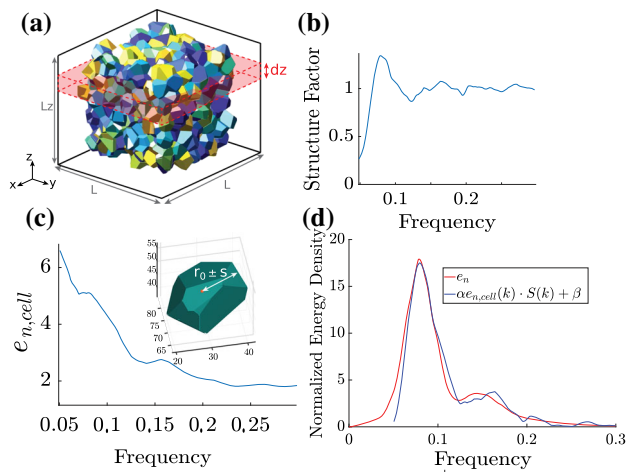
Fig. 3 Relation between the normalized energy density and the form and structure factors of cells in a simulated aggregate. **a** From the Voronoi tessellation each cell in the image volume could be individually segmented to obtain both its centroid and its associated cell form factor. **b** Structure factor computed from the centroid obtained from **a**. **c** Cell form factor averaged from all the cells segmented in **a**. **d** Comparison of the energy density of the cell image and the average cell form factor multiplied by the structure factor, both quantities show a linear relationship with a coefficient $\alpha = 3.45$ and $\beta = -6.15$

Fig. 4 The Fourier analysis provides accurate estimates of cell size down to a field of view containing 3 cells in each directions. **a** Shape of the normalized energy density as a function of the size L. As expected, the peaks become smaller and wider when L decreases. **b** Blue: mean error $(D_F - D_V)/D_V$ in % and its associated standard deviation calculated on a batch of 11 3D images as a function of the size L ($r_0 = 5$, σ between 0 and 2). Red: same for $(D'_F - D_V)/D_V$. Blue and red points are slightly shifted for the sake of clarity

We obtained $\alpha = 3.45$ and $\beta = -6.15$ (Fig. 3d). The fact that we do not get $\alpha = 1$ and $\beta = 0$ [as expected from Eq. (6)] may arise from the conjunction of different reasons. Firstly, cross-correlations between the shape and structure factors are expected, as cells are deformable objects packed in the aggregate. Secondly, the cell shape factor is accounting twice for each cell facet (see material and methods). Lastly, but maybe the most important reason, this adjustment may originate from finite size effects, the numerical Fourier transform being a truncated version of the analytical one. However Fig. 3d still shows that the Fourier energy density is well rationalized using the product of the average cell form factor and the structure factor. Thus it clearly appears that the peak in e_n corresponds to the first peak of the structure factor.

3.3 Effect of experimental parameters on cell size measurements

Below, we evaluate the robustness of the Fourier analysis to provide an accurate measurement of the mean cell size as a function of the modeled acquisition parameters (defined on Fig. 3a, c). For all the following results, a set of 11 3D-images generated with $r_0 = 5$ (i.e., an average cell diameter $D_V = 10$ pixels) were used. We varied sequentially the number of images per field of view by varying the image size $L \times L \times L_z$, the pixel size in z (dz) and the sample thickness L_z.

3.3.1 Effect of the number of cells per field of view

For obtaining a nice peak in the Fourier space, there should be a sufficient number of cells in each image; the cell volume itself is not as crucial as long as it is still measurable, as we already demonstrated in 2D [9]. The higher the number of visible wavelengths, the stronger the peak at that corresponding frequency in Fourier space will be (see Fig. 4b). The influence of the cell number and, more specifically, the quantification of the minimal number of cells required for the effectiveness of the Fourier analysis were investigated.

In this section, we took $dz = 1$ and $L_z = L$, and the mean error on cell size measurement was investigated as a function of L (Fig. 4b). As cell size was kept constant, this resulted in varying the number of cells in the image.

Even up to $L = 32$ pixels, the mean error remained close to zero with standard deviation around 3%. As the cell size is set around 10 pixels, this indicates that having 3 cells in each direction is enough to obtain a valid result. Therefore, this method is efficient to accurately provide the mean cell size even with high-magnification images where the number of cells in the field of view is reduced.

The direct measure of the peak position is quite sensitive to the shape of the curve and can unfortunately be fitted by a Gaussian for a subpixel accuracy, and this may induce imprecise measurements of cell size. So, the
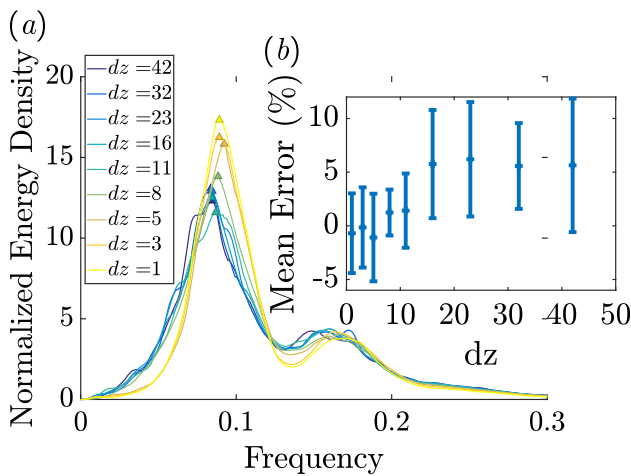
Fig. 5 The pixel size in z only influences the measurement if it becomes of the order of the cell size. **a** Shape of the normalized energy density as a function of frequency for in-depth pixel size dz. **b** Mean error $(D_f - D_V)/D_V$ in % and its associated standard deviation calculated on a batch of 11 3D images as a function of the in-depth pixel size dz ($r_0 = 5$, σ between 0 and 2, $L = 128$)

position of the weighted peak was also calculated:

$$f_{peak} = \frac{\int_{f_1}^{f_2} k * e_n(k)\, dk}{\int_{f_1}^{f_2} e_n(k)\, dk} \tag{9}$$

with f_1 and f_2 the frequencies at half height of the principal peak. Equation (9) thus leads to a mean cell diameter $D'_F = 1/f_{peak}$. Figure 4b shows that the cell diameter calculated by this latter technique provides slightly underestimated values compared to the direct measure of the peak position. Still, this method is more robust as the values calculated with this technique appear less dispersed.

3.3.2 Effect of the pixel size in z (dz)

In image acquisition, one of the hardest things to achieve is a high resolution in z-axis direction. So far, the resolutions in x, y and z we used were identical. However, experimentally the distance between z planes dz is twice or even four times larger than the resolution in the x-y plane. The influence of the in-depth resolution on cell size measurements was tested by removing information from a simulated 3D image with $128 \times 128 \times 128$ pixels. Only one slice every dz was kept, dz representing the pixel size in z. As shown in Fig. 5b, when dz is of the order of the cell size (10 pixels here), the results are biased and the size measurements are overestimated with a larger error. This result suggests that this method keeps accurate even
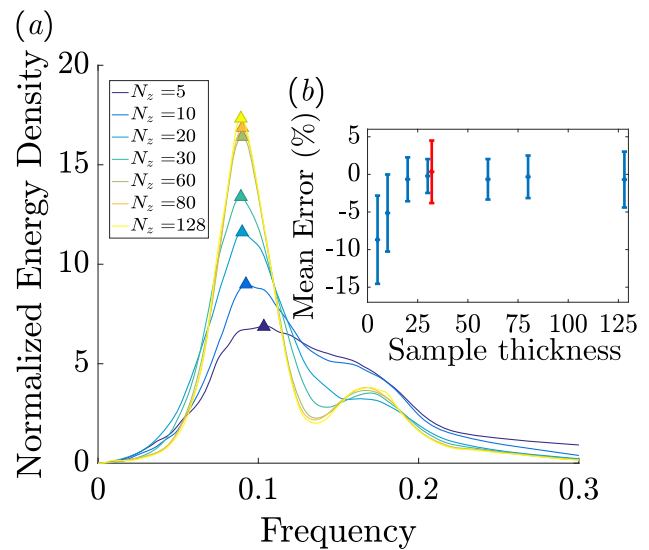

Fig. 6 Influence of the number of z-slices in the stack on the accuracy of the calculated cell size. **a** Shape of the normalized energy density as a function of frequency for different numbers of z slices. As expected, the peaks become smaller and wider, while this number decreases. **b** Mean error and its associated standard deviation calculated on a batch of 11 3D images as a function of the number of z slices in the stack ($r_0 = 5$, σ between 0 and 2, $L = 128$). Blue points, $dz = 1$. Red point: $dz = 10$

with low-magnification objectives and does not require high-resolution microscopy.

3.3.3 Effect of sample thickness L_z

Experimentally, the total number of z planes in the stack is often significantly lower than the total number of pixels in x and y directions. We thus wondered whether 3D imaging is necessary or whether a single cross section could be enough to accurately measure the mean cell size. Here we used $dz = 1$ and varied the value of L_z. Figure 6 shows that as the number of z planes decreases, the results become more and more biased. The cells appear smaller than they really are (which is consistent as within a single plane, many sliced cells are visible, that appear smaller than they really are). Consistent with Sect. 3.3.1, the optimal number of slices to get accurate measurement is about 30, which corresponds to about three cells in the z direction. Altogether, our data suggest that to get a proper measurement of cell size, it is enough to have stacks containing only 3 cells in all directions, with an in-depth resolution of the order of the cell size (thus a 3D stack of 4 images). Figure 6b shows the accuracy of the measure in these conditions (red point). The mean error is close to zero although the standard deviation is slightly larger than for a more resolved imaging.
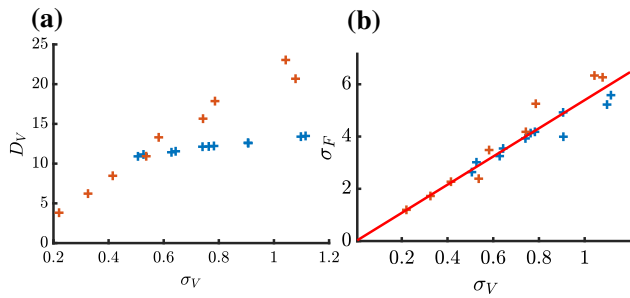
Fig. 7 The standard deviation of the cell size distribution can be calculated from the normalized energy density spectrum [Eq. (10)]. **a** Width of the size distribution as a function of the average size for two different sets of artificial images (in red and in blue). **b** Proxy for the width of the distribution obtained from the Fourier analysis [Eq. (10)] as a function of the actual width obtained from segmented images. Both correlate linearly, with a slope $a = 5.4$ (red line). Determination coefficient of 0.9

4 Measuring the standard deviation of the size distribution

The quantification of the standard deviation of the cell size distribution was addressed empirically. Because the width of a distribution is proportional to the mean size for a given set of simulated data (Fig. 7a) which may lead to undesired correlations, two different batches of simulated data were considered. In the first set of data, the distribution of the distance between the Voronoi seeds was a Dirac function, whose center was varied. In the second set, the distribution was a Gaussian with a given mean distance and the width of the distribution was varied. We show that for both ways of generating the Voronoi cells, a good proxy for the quantification of the standard deviation of the cell size distribution is:

$$\sigma_F = 1/f_1 - D'_F \qquad (10)$$

where f_1 is the frequency at half height on the left of the principal peak, $f_1 < f_{D'_F}$. σ_F was compared to the known standard deviation of the size distribution σ_V (Fig. 7b). A linear correlation between σ_V and σ_F was obtained with a high correlation coefficient. This validates the use of Eq. (10) to quantify cell size dispersion as σ_F/a ($a = 5.4$ being the proportionality coefficient between σ_F and σ_V see Fig. 7).

5 Results on two-photon stacks of cellular aggregates

In the previous section, we evaluated the performance of the algorithm on simulated 3D data. In this section, we tested its performance on real data. Cellular aggregates of HT29 cells were incubated with a fluorophore that only penetrates in the interstitial space between each cells. Two-photon microscopy was used for imag-
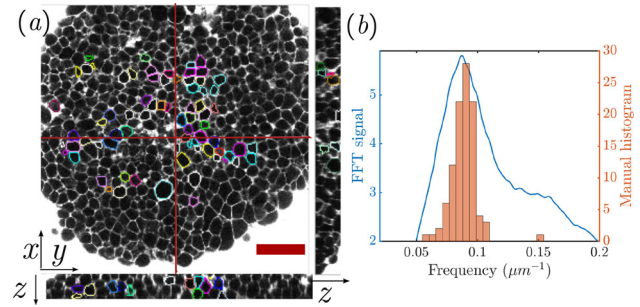

Fig. 8 The Fourier analysis accurately determines cell size of real data. **a** Projections of a two-photon stack of a cellular aggregate in (xy), (xz), and (yz). (xz) and (yz) projection were taken along the red lines drawn in the (xy) plane. Bar: 50 µm. Cells segmented manually using Amira software are encircled with colors. **b** Superimposition of the histogram of $1/D_V$ obtained manually (orange bins) and of $1/D_F$ obtained with the FFT signal (blue line)

ing (Fig. 8). Energy density function [Eq. (2)] was computed (a few seconds of computation). In parallel, 100 cells of the dataset were manually segmented using Amira software (a few hours of segmentation) (Fig. 8a). Figure 8b shows that the Fourier analysis fits remarkably well with the calculation from the manual segmentation. The mean size of the manually segmented cells was of $11.40 \pm 1.38\,\mu m$ (average value $\pm$ standard deviation), whereas the measurement from the Fourier analysis gave $11.50 \pm 1.37\,\mu m$. The latter standard deviation was obtained following Eq. (10) as $\sigma_F/5.4$.

6 Local measurements on an aggregate compressed in between two plates (cylindrical geometry)

A cellular aggregate was positioned in a microfluidic channel. Confinement in the channel imposed a cylindrical shape (Fig. 9a). The in-plane radius was examined in response to an osmotic shock (see [12] for details). Variation of the osmotic pressure provoked a decrease in size of the whole aggregate and of the individual cells. We tested the Fourier analysis to quantify the difference in cell size assuming that the number of cells remains constant in the aggregate during the experiment (which is a valid assumption as the compression only lasts half an hour). First, the initial radius of the spheroid R_{before} and its final radius after compression R_{after} were measured. A ratio of $R_{\text{after}}/R_{\text{before}} = 0.937$ was obtained (Fig. 9b). Ratio of the mean cell sizes obtained with the Fourier analysis gave consistent results: $D'_{\text{after}}/D'_{\text{before}} = 0.937$ (Fig. 9c). We finally show that local measurements are indeed feasible; as explained in Sect. 2.5, we calculated the cell size as a function of the radial distance to the center using subimages of size L=128 pixels, $Lz = 39$ (initial image size $512 \times 512 \times 39$). We observe a significant decrease in size toward the cell center (Fig. 9d). This
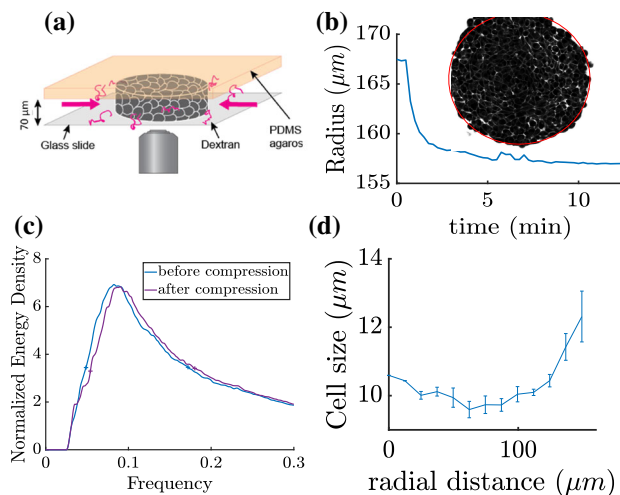
Fig. 9 The Fourier analysis is undisturbed by the global shape of the aggregate, measure small variations of cell size and can be applied on subimages to get local measurements. **a** A HT29 aggregates are confined in a microfluidic chamber and submitted to an osmotic shock as done in [12]. **b** The aggregate radius is tracked during the shock. After segmentation a circle is fitted to the aggregate global shape. The ratio of the radii before and after the shock is $R_{\mathrm{after}}/R_{\mathrm{before}} = 0.937$. **c** Normalized energy density as a function of frequency before (blue) and after (violet) the osmotic shock. Difference in size is identical to the macroscopic measurement : $D'_{\mathrm{after}}/D'_{\mathrm{before}} = 0.937$. **d** The Fourier algorithm was applied locally on subimages disposed on a polar grid (r, θ) (r being the distance from the aggregate center). The results were averaged along θ. Cell size is plotted as a function of this radial distance

result then showed that (i) the Fourier analysis can handle a cylindrical symmetry, and (ii) it allows addressing variations of the size of few % and (iii) can be applied locally for a getting a spatial map of cell size inside the aggregate.

7 Conclusions

We present here an original method based on Fourier transform to calculate the mean cell size and the width of its distribution very accurately. This method exploits the fact that the Fourier transformation of the fluorescent signal gives a pattern that can be analyzed with tools from elastic scattering theory. A first observation is the isotropic scattering pattern of spherical symmetry, which supports the intuition that cells in 3D aggregates have a weak positional order. The originality of the method is to analyze the power spectral density not renormalized by the spectral volume. This allows enhancing signals that are away from the center of the scattering pattern. Then, the position of the first peak can be accurately measured, giving access to an accurate quantification of the cell mean diameter. While, in principle, the scattering pattern could provide finer

information on the mean form of the cells or on their positional order, this information relies on the use of interaction models. To the best of our knowledge, such models do not exist for cellular organizations yet, thus limiting the exploitation of the diffusion pattern. However, an empirical approach was proposed to obtain the width of the size distribution, which will gain being confirmed by theoretical modeling.

The accuracy of this new tool was tested thoroughly in regard to experimental conditions. For instance, we show that a volume of $3 \times 3 \times 3$ cells is enough to obtain an accurate quantification of the cell size, with error below 5%. We indeed show that very local measurements could be performed. Moreover, our tool does not require a very high z resolution nor a very large field of view to get accurate measurements. It is interesting to note that one single set of data can be used several time with different sectioning (varying dz for example) to get different measurements of the peak location. Then, the averaged result gives an even more accurate quantification. There is no doubt that this technique can also be applied in vivo when automatic cell segmentation is too difficult to perform as in the data presented here. Further development could enclose the study of cell anisotropy, which would necessitate fitting the data by an ellipse instead of a sphere.

References

1. E. Zlotek-Zlotkiewicz, S. Monnier, G. Cappello, M. Le Berre, M. Piel, J. Cell Biol. **211**(4), 765 (2015). https://doi.org/10.1083/jcb.201505056
2. M. Guo, A.F. Pegoraro, A. Mao, E.H. Zhou, P.R. Arany, Y. Han, D.T. Burnette, M.H. Jensen, K.E. Kasza, J.R. Moore, F.C. Mackintosh, J.J. Fredberg, D.J. Mooney, J. Lippincott-Schwartz, D.A. Weitz, Proc. Natl. Acad. Sci. U.S.A. **114**(41), E8618 (2017). https://doi.org/10.1073/pnas.1705179114
3. E.K. Hoffmann, I.H. Lambert, S.F. Pedersen, Physiol. Rev. **89**(1), 193 (2009). https://doi.org/10.1152/physrev.00037.2007
4. N. Perez Gonzalez, J. Tao, N.D. Rochman, D. Vig, E. Chiu, D. Wirtz, S.X. Sun, Mol. Biol. Cell **29**(21), 2591 (2018). https://doi.org/10.1091/mbc.E18-04-0213
5. C. Cadart, E. Zlotek-Zlotkiewicz, L. Venkova, O. Thouvenin, V. Racine, M. Le Berre, S. Monnier, M. Piel, Methods Cell Biol. **139**, 103 (2017). https://doi.org/10.1016/BS.MCB.2016.11.009

6. A.K. Bryan, A. Engler, A. Gulati, S.R. Manalis, PLoS One **7**(1), e29866 (2012). https://doi.org/10.1371/journal.pone.0029866

7. F. Bosveld, I. Bonnet, B. Guirao, S. Tlili, Z. Wang, A. Petitalot, R. Marchand, P.L. Bardet, P. Marcq, F. Graner, Y. Bellaiche, Science **336**(6082), 724 (2012). https://doi.org/10.1126/science.1221071

8. P. Marmottant, A. Mgharbel, J. Käfer, B. Audren, J.P. Rieu, J.C. Vial, B. van der Sanden, A.F.M. Marée, F. Graner, H. Delanoë-Ayari, Proc. Natl. Acad. Sci. USA **106**(41), 17271 (2009). https://doi.org/10.1073/pnas.0902085106

9. M. Durande, S. Tlili, T. Homan, B. Guirao, F. Graner, H. Delanoë-Ayari, Phys. Rev. E **99**(6), 062401 (2019). https://doi.org/10.1103/PhysRevE.99.062401

10. R. Bracewell, *The Fourier Transform and its Applications* (McGraw-Hill Book Company, 1986). http://www.academia.edu/download/44001876/34957138.pdf

11. E.C. Costa, A.F. Moreira, D. de Melo-Diogo, V.M. Gaspar, M.P. Carvalho, I.J. Correia, Biotechnol. Adv. **34**(8), 1427 (2016). https://doi.org/10.1016/j.biotechadv.2016.11.002

12. M.E. Dolega, S. Monnier, B. Brunel, J.F. Joanny, P. Recho, G. Cappello, Elife **10**, 1 (2021). https://doi.org/10.7554/eLife.63258

13. L. Moisan, J. Math. Imaging Vis. **39**(2), 161 (2011). https://doi.org/10.1007/s10851-010-0227-1

14. M. Frigo, S.G. Johnson, in *ICASSP, IEEE International Conference on Acoustics, Speech and Signal Processing—Proceedings*, vol. 3 (IEEE, 1998), pp. 1381–1384. https://doi.org/10.1109/ICASSP.1998.681704

15. D.J. Kinning, E.L. Thomas, Macromolecules **2**(5), 1712 (1984). https://doi.org/10.1021/ma00139a013

16. N.W. Ashcroft, N.H. March, Proc. R. Soc. Lond., Ser. A. Math. Phys. Sci. **297**(1450), 336 (1967)

17. J.S. Pedersen, Adv. Colloid Interface Sci. **70**(1–3), 171 (1997). https://doi.org/10.1016/S0001-8686(97)00312-6